

An X-ray study of the galactic-scale starburst-driven outflow in NGC 253

Ikuyuki MITSUISHI^{1,2}, Noriko Y. Yamasaki², Yoh Takei²

¹ *Department of Physics, Tokyo Metropolitan University, 1-1 Minami-Osawa Hachioji Tokyo 192-0397 JAPAN*

² *Institute of Space and Astronautical Science, Japan Aerospace Exploration Agency (ISAS/JAXA),*

3-1-1 Yoshinodai, Chuo-ku Sagamihara, Kanagawa, 252-5210

mitsuisi@phys.se.tmu.ac.jp

(Received 2012 July 23; accepted 2012 December 3)

Abstract

X-ray properties of hot interstellar gas in a bright, nearby edge-on starburst galaxy NGC 253 were investigated to gain a further understanding of starburst-driven outflow activity by *XMM-Newton* and *Suzaku*. Spectroscopic analysis for three regions of the galaxy characterized by multiwavelength observations i.e., the superwind region, the disk region and the halo region, was conducted. Various emission lines from O, Ne, Mg, Si and Fe were observed in the spectra of each region. The hot gas was represented by two thin thermal plasmas with temperatures of $kT \sim 0.2$ and ~ 0.6 keV. Abundance ratios i.e., O/Fe, Ne/Fe, Mg/Fe and Si/Fe, are consistent between three regions, which suggests the common origin of the hot gas. The abundance patterns are consistent with those of type II supernova ejecta, indicating that the starburst activity in the central region provides metals toward the halo through a galactic-scale starburst-driven outflow. The energetics also can support this indication on condition that 0.01–50 $\eta^{1/2}$ % of the total emission in the nuclear region has flowed to the halo region. To constrain the dynamics of hot interstellar gas, surface brightness and hardness ratio profiles which trace the density and temperature were extracted. Assuming a simple polytropic equation of state of gas, $T\rho^{1-\gamma} = \text{const}$, we constrained the physical condition. γ is consistent with 5/3 at the hot disk of <3 kpc from the center along with the minor axis and T is constant ($\gamma = 1$) in the halo whose distance is between 3 and 10 kpc from the center. It is suggested that the hot gas expands adiabatically from the central region towards the halo region while it moves as free expansion from the inner part of the halo towards the outer part of the halo as the outflow. We constrained the outflow velocity to be $>100 \text{ km s}^{-1}$ from the observed temperature gradient in the halo. In comparison with the escape velocity of $\sim 220 \text{ km s}^{-1}$ for NGC 253, it is indicated that the hot interstellar gas can escape from the gravitational potential of NGC 253 by combining the outflow velocity and the thermal velocity.

Key words: starburst, X-ray, NGC 253

1. Introduction

It has long been known that the intergalactic medium contains substantial amount of metals (e.g., Songaila & Cowie (1996); Aguirre et al. (2001)). The metals are thought to originate from stars in galaxies. However, the mechanism of how the metals are expelled from the galaxies to an intergalactic space is still not clear and arguable. Galactic-scale outflows have been regarded to play an important role in transporting materials into the intergalactic space. As a power source of galactic-scale outflows, starburst activity is one of the most plausible candidates (e.g., Strickland (2002); Heckman (2003); Veilleux et al. (2005)). Some galaxies have been experiencing starbursts (e.g., Kennicutt (1998); Strickland et al. (2004)) and starburst activity itself is considered to be common and universal in a life of a galaxy (e.g., Pettini et al. (2001); Shapley et al. (2003); McQuinn et al. (2010)). According to a scenario of a galactic-scale starburst-driven outflow, thermal pressure builds up in an interstellar medium (ISM) of a galaxy due to a supernova shock and then removes a fraction of the ISM (Veilleux et al. 2005). Finally, hot gas expands and breaks out of the disk and the halo of the host galaxy as the outflow, if the pressure is large enough to escape the gravitational potential of the disk and the host galaxy. This heated outflowing hot gas emits mainly X-rays and therefore X-rays can be a tracer of outflowing hot gas itself. To test this scenario observationally, chemical abundance is a good probe because great deal of type II supernovae produced by massive stars associated with starburst activity provide abundant α elements selectively. Recently, abundance patterns for several starburst galaxies, i.e., NGC 4631, M82 and NGC 3079, were reported (Yamasaki et al. 2009; Konami et al. 2011; Konami et al. 2012). α elements such as O, Ne, Mg, Si and S are observed abundantly even outside the disk and they argue that the observed ISM outside the disk originates from the inner starburst region contaminated by type II supernovae. However, abundance patterns were not accurately constrained in some of previously studied galaxies due to poor statistics of NGC 4631 and NGC 3079 except for a central region and contamination of charge-exchange emission in M82 disk. To pursue the origin of hot gas in the halo chemically, a continuous measurement of abundance patterns from the inner starburst region to the halo is important.

NGC 253 is a bright nearby well-studied starburst galaxy. The edge-on orientation and its large apparent diameter make it a suitable target to study the spatial distribution of emission features and the outflow from galaxies. Actually, the 100 pc-scale outflow of ionized gas nearby the nuclear region with velocity of 100–300 km s⁻¹ is reported by an H α observation (Westmoquette et al. 2011). This H α outflow is very similar in morphology to the known X-ray emitting hot gas on scales down to ≤ 20 pc (Strickland et al. 2000). *AKARI* revealed that NGC 253 holds a uniquely-shaped far-infrared halo reaching out to ~ 9 kpc perpendicular to the disk region (Kaneda et al. 2009). Interestingly, the FIR halo clearly traces an X-ray emitting gas (Bauer et al. 2008), which suggests that dust in the halo comes from the inner region together with X-ray emitting hot gas. In Kaneda et al. (2009), they estimate an averaged dust outflow velocity to be 300–2000 km s⁻¹ and predict that dust would be escaping from the gravitational potential of NGC 253.

Mitsuishi et al. (2011) studied intensively the central disk of NGC 253 with *Chandra*, *XMM-Newton* and *Suzaku*. The hard X-ray emitting gas associated with the densest molecular clouds (Sakamoto et al. 2011) are suggested to originate from the starburst activity. This central hot gas can be a source of hot gas observed outside the nuclear region through the outflow. In this paper, we analyze X-ray emission from whole NGC 253 with *XMM-Newton* and *Suzaku*, to verify the galactic-scale starburst-driven outflow chemically. We extract abundance patterns for three characteristic regions of NGC 253 and discuss the origin of hot gas in the halo region. Then, we also constrain physical conditions of hot gas in the disk and the halo regions and finally discuss the possibility of the outflow toward the intergalactic space.

Throughout this paper, we adopt the distance of 3.4 Mpc (Dalcanton et al. 2009) to NGC 253 which corresponds to $16 \text{ pc arcsec}^{-1}$ at the redshift of 8.1×10^{-4} . Unless otherwise specified, all errors are at 90 % confidence level in text and tables, and at 1σ in figures.

2. Observations & Data Reduction

To pursue the origin of hot gas in the halo region, we studied three regions in NGC 253 characterized by multiple wavelength observations as shown in Figure 1. The first one is a region (hereafter the *superwind* region) where an outflowing ionized gas is detected in the $\text{H}\alpha$ observation (Westmoquette et al. 2011) with velocity of $100\text{--}300 \text{ km s}^{-1}$ from the central region toward an outside perpendicular to the disk of the order of several 100 pc. This outflow is considered to originate from the nuclear region. Thus, we extracted the $1.4 \times 0.9 \text{ kpc}^2$ area including this outflow region. The second one is a region (the *disk* region) characterized by optical B band which is mainly attributed to massive stars associated with the starburst activity. The optical disk region is elliptically distributed with major/minor axes of $14 \times 3 \text{ kpc}^2$ (Pence 1980). We adopted this optical disk region as the *disk* region. The last one is a region (the *halo* region) characterized by a diffuse FIR emission extending up to 9 kpc perpendicular to the disk (Kaneda et al. 2009). From its spatial coincidence with an X-ray emitting plasma, the extended FIR emission is considered to be transported from the central starburst region into the halo by the outflow associated with the starburst activity. The *halo* region was outside the *disk* region ($15 \times 7.4 \text{ kpc}^2$).

For spectral analysis of the *superwind* region and the *disk* region, we utilized *XMM-Newton*. *XMM-Newton* has the angular resolution of $\sim 10''$ corresponding to $\sim 160 \text{ pc}$, which is beneficial in removing a contamination from point sources and extracting abundance patterns accurately with a good sensitivity for soft emission lines. For spectral analysis of the *halo* region, *Suzaku* was used because the lowest and stable background are optimum to study the faint soft X-ray emission from the halo. The faint soft X-ray emission from the halo region extends out to $\sim 10 \text{ kpc}$ perpendicular to the disk, which makes it difficult to estimate the X-ray background emission from the same *Suzaku* FOV. Therefore, we use an offset observation to evaluate the X-ray background emission. The offset region covers just next to the *halo* region of NGC 253. We also extracted spectra from archival *Chandra* data for the three regions. However, due to lack of sensitivity below 1 keV, the emission lines cannot

be clearly detected. Therefore, we concentrate on *XMM-Newton* and *Suzaku* data in this paper. The sequence numbers, observation dates, pointing directions and exposure times are summarized in Table 1.

For spectral analysis using *XMM-Newton*, we removed flaring high background periods in which the count rate is over 0.35 above 10 keV. The redistribution matrix files (RMFs) and Ancillary response files (ARFs) were made by the Science Analysis System `rmfgen` and `arfgen` tools. We extracted the background from a source-free region. In spectra of the *disk* region, two strong instrumental fluorescent emission lines of Al (1.49 keV) and Si (1.74 keV) were not subtracted properly. Since the first line was subtracted too much which gave rise to a large residual around 1.49 keV, we ignored the energy band between 1.45 keV and 1.55 keV. On the other hand, because the second fluorescent line was not subtracted enough, we added a gaussian component to make up for this residual fixing the line center at 1.74 keV. We did not ignore this energy band in order to evaluate the abundance of Si. In spectra of the *superwind* region, no instrumental fluorescent line feature was found since the emission from the ISM was much brighter than that of the background.

For spectral analysis of *Suzaku*, RMFs were produced by `xisrmfgen` ftool to calculate time-dependent XIS response considering secular degradation of the XIS energy resolution. ARFs were also created using `xissimarfgen` (Ishisaki et al. 2007). For spectral analysis of both the *halo* region and the offset region, we adopted a uniform circle with a radius of 20' as an input image to `xissimarfgen`. For the non X-ray background (NXB) component, an accumulated dark Earth database with `xisnxbgen` ftool was used (Tawa et al. 2008).

In this paper, a neutral hydrogen column density of the Galaxy is assumed to be 1.5×10^{20} cm⁻², based on the LAB survey (Kalberla et al. 2005). We assume the solar abundance tabulated in Anders & Grevesse (1989). HEASoft version 6.11 and XSPEC 12.7.0 were utilized.

Table 1. Observation log

		<i>Suzaku</i>		<i>XMM-Newton</i>
		NGC 253	NGC 253 OFFSET	NGC 253
Sequence number		805018010	803004010	0152020101
Obs date		2010/12/14–16	2008/12/29–30	2003/06/19–20
FOV center	($\alpha_{2000}, \delta_{2000}$)	(00:47:26, -25:13:46)	(00:48:22, -25:02:51)	(00:47:37, -25:18:10)
Exposure	ks	101	57	76*

* Exposure time after a background flare removal.

3. Analysis & Results

3.1. Spectral analysis in the *superwind* region and the *disk* region

We extracted the spectrum in the *superwind* and *disk* regions as shown in Figure 1. For spectral analysis of the *disk* region, we removed central 90'' region to exclude the *superwind* region.

Point sources were also removed with a radius of 10".

Spectra after background subtraction were fitted with emissions from absorbed hot interstellar gas and a sum of unresolved point sources. As absorbers, Galactic and intrinsic absorptions were taken into account. The former was fixed to the Galactic value while the latter was set to be free. Optically thin thermal collisionally-ionized equilibrium (CIE) plasma was used to express the hot gas. Metal abundances in a plasma were divided into five groups, i.e., O, Ne, (Mg & Al), (Si, S, Ar & Ca) and (Fe & Ni), based on the metal synthesis mechanism of supernovae. The abundance of each group is set to be free. For the hot interstellar gas component, we tried a two-temperature plasma model. A one-temperature model cannot reproduce the spectrum due to large residuals around emission lines such as O and Fe. No improvement in the fit was seen when the third-temperature plasma was added. Metal abundances between the plasmas was linked to each other assuming the same origin of the hot gas in the extracted region. Bremsstrahlung was used to represent the emission from a sum of point sources. The temperature of the bremsstrahlung was fixed to the typical temperature of 10 keV of the low mass X-ray binary, responsible for the emission from the point sources (Yamasaki et al. 2009). These components were modeled by $phabs_{\text{Galactic}} \times phabs_{\text{superwind or disk}} \times (vapec_{2T: \text{superwind or disk}} + zbrems_{\text{superwind or disk}})$ in the XSPEC software. $phabs_{\text{superwind or disk}}$, $vapec_{2T: \text{superwind or disk}}$ and $zbrems_{\text{superwind or disk}}$ correspond to the absorption column density, a two-temperature thermal plasma and the bremsstrahlung component in the *superwind* region or the *disk* region, respectively.

Resultant spectra and the best fit parameters are shown in Figure 2 and summarized in Table 2. The best fit temperatures of the two regions are both ~ 0.2 keV and ~ 0.6 keV. For the spectrum of the *disk* region, we ignored the fluorescent Al $K\alpha$ energy band and the gaussian component was added to make up for the neutral Si K fluorescent emission line. We extracted abundance ratios for the best fit model in both regions by two-parameter confidence contours between each α element and Fe. Then, we converted the abundance ratio to a number ratio of the α element to the Fe atom using the abundance table that we adopted. Note that the number ratio is independent of the abundance table that we assumed in the fit. Resulting number ratios are exhibited in Figure 3. Abundance patterns of each element in the two regions are consistent. As comparisons, the number ratios for the solar abundance that we adopted, SN II and SN Ia products are also plotted. For SN II products, we referred to those of an average over the Salpeter initial mass function of stellar mass from 10 to 50 M_{\odot} in Nomoto et al. (2006) with a progenitor metallicity of $Z = 0.02 Z_{\odot}$. As SN Ia yields, we referred to the W7 model in Iwamoto et al. (1999).

3.2. Spectral analysis in the halo region

3.2.1. Evaluation of the X-ray background emission

For spectral analysis of the *halo* region, *Suzaku* data were utilized. Firstly, we analyzed the data of the offset region to evaluate the X-ray background emission. The offset region is located just next to NGC 253 as shown in Figure 1. We removed point-source candidates and diffuse-like

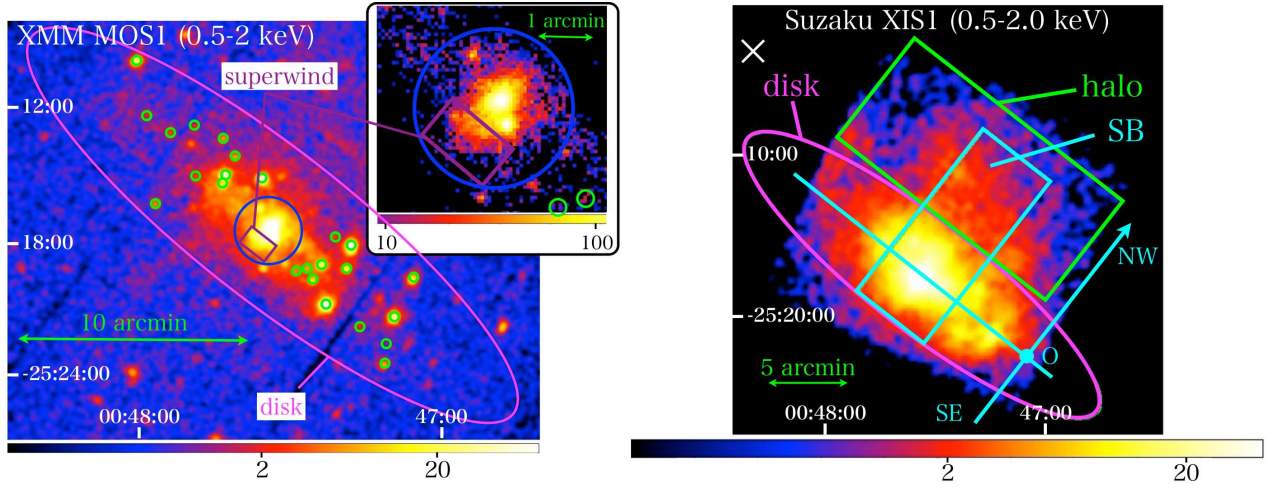


Fig. 1. Left: *XMM-Newton* MOS1 image in 0.5–2.0 keV in the unit of $\text{cts} (76 \text{ ks})^{-1} (80 \text{ pixel})^{-1}$. A close-up view of the *superwind* region is also exhibited in upper right. Purple rectangle and magenta ellipse show the regions to extract abundance patterns denoted as the *superwind* and *disk* regions in this paper, respectively. Blue and green circles correspond to the excluded regions in spectral analysis of the *disk* region. Right: *Suzaku* XIS1 image in 0.5–2 keV in the unit of $\text{cts} (101 \text{ ks})^{-1} (64 \text{ pixel})^{-1}$. Green rectangle is the *halo* region used for the spectral analysis in §3.2, and the surface brightness and the hardness ratio extracted from the cyan region denoted as the *SB* region are used in §3.3. White cross mark shows the aim point of the offset region. The images of *Suzaku* and *XMM-Newton* are smoothed to emphasize extended sources with kernels of $\sigma = 25''$ and $12''$, respectively but no smoothing is applied for the close-up image. The scale is logarithmic. Vignetting and background are not corrected for.

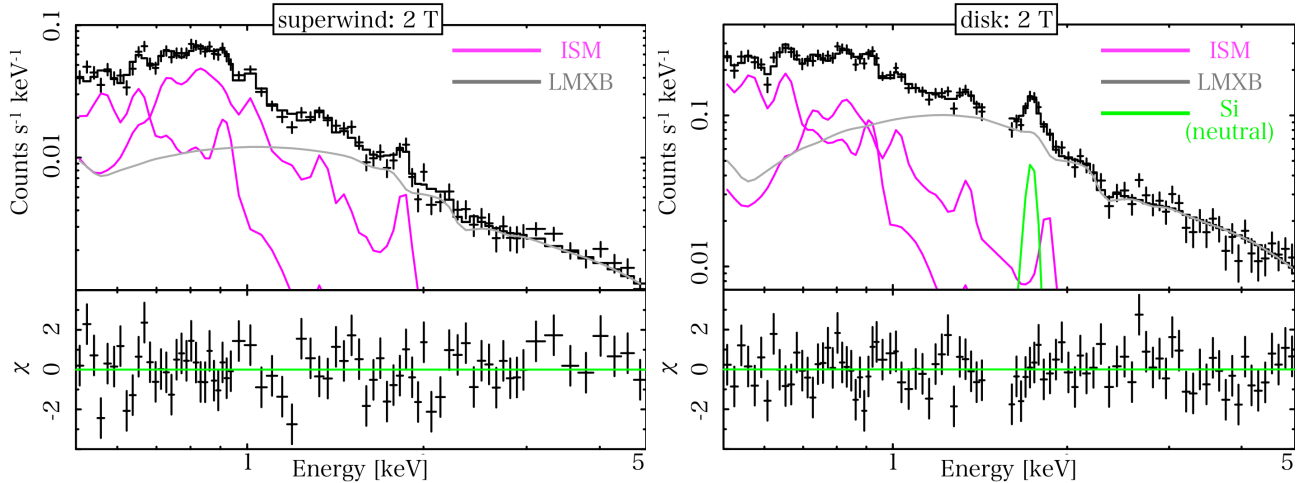


Fig. 2. Spectra obtained by *XMM-Newton* MOS detector at the energy band of 0.5 and 5 keV in the *superwind* (left) and *disk* (right) regions fitted with the two-temperature model. Magenta and gray lines correspond to the best fit model for hot interstellar gas and a sum of point sources, respectively. We ignored the energy band in 1.45–1.55 keV and added the gaussian component (green) in the spectrum of the *disk* region due to the detector background of the neutral Al and Si K fluorescent emission lines, respectively.

sources by a visual inspection and a wavelet algorithm (by a CIAO tool *wavdetect*) in 0.4–2.0 keV. We fitted the spectrum with the typical X-ray background emission expressed by a sum of (1) an unabsorbed thin thermal CIE plasma, (2) an absorbed thin thermal CIE plasma and (3) an absorbed

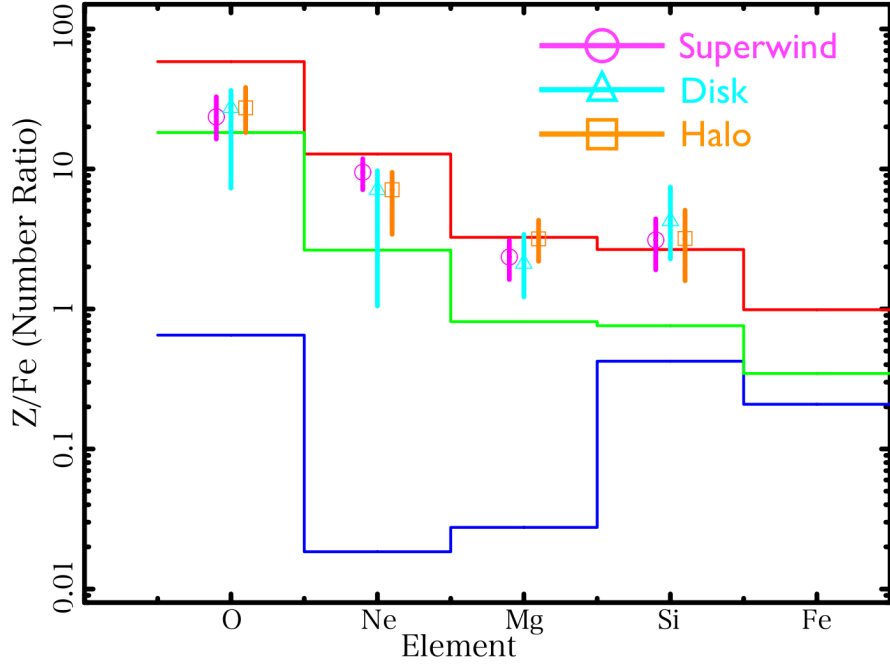


Fig. 3. Abundance patterns of O/Fe, Ne/Fe, Mg/Fe and Si/Fe obtained from spectral analysis in the *superwind* region (magenta), the *disk* region (cyan) and the *halo* region (orange), respectively. Blue, green and red lines show expected products by type I supernova (Iwamoto et al. 1999), solar abundance tabulated in Anders & Grevesse (1989) as an example of solar abundance tables and type II supernova (Nomoto et al. 2006).

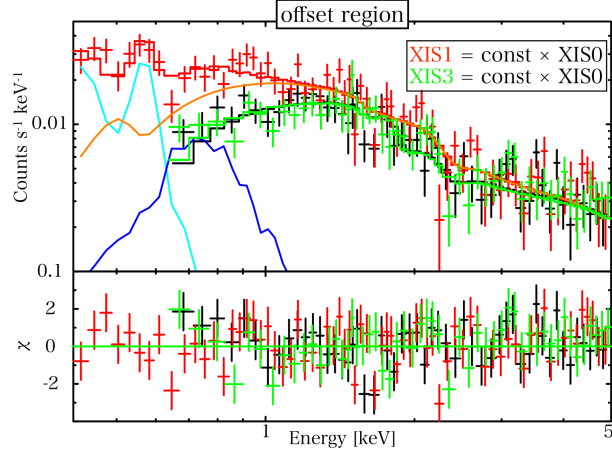


Fig. 4. Spectrum obtained in the offset region fitted with the typical X-ray background emission model, i.e., $apex_{SWCX+LHB}$ (cyan) + $phabs_{Galactic} \times (apex_{MWH}$ (blue) + $power-law_{CXB}$ (orange)). Three components correspond to SWCX+LHB, MWH and CXB, respectively. For simplicity, the best fit model is shown for only the XIS1 detector. For spectra of the XIS1 and XIS3 detectors, the constant factor is multiplied to consider the systematic error in different sensors.

Table 2. Best fit parameters for the *superwind* region and the *disk* region by *XMM-Newton*.

Region	<i>Superwind</i>	<i>Disk</i>
Model	$2T$	$2T$
$N_{\text{H } phabs:Galactic}$ ($\times 10^{21}$ [cm $^{-2}$])	0.15 (fix)	0.15 (fix)
$N_{\text{H } phabs:superwind \text{ or } disk}$ ($\times 10^{21}$ [cm $^{-2}$])	<0.5	$1.0^{+1.4}_{-0.9}$
$kT_{vapec1:superwind \text{ or } disk}$ [keV]	0.21 ± 0.02	0.20 ± 0.02
O [Z_{\odot}]	$0.44^{+0.60}_{-0.20}$	$0.28^{+0.33}_{-0.09}$
Ne [Z_{\odot}]	$1.3^{+0.99}_{-0.53}$	$0.51^{+0.79}_{-0.21}$
Mg, Al [Z_{\odot}]	$1.0^{+1.1}_{-0.6}$	$0.49^{+0.92}_{-0.26}$
Si, S, Ar, Ca [Z_{\odot}]	$1.4^{+1.1}_{-0.8}$	$1.1^{+1.6}_{-0.6}$
Fe, Ni [Z_{\odot}]	$0.35^{+0.38}_{-0.14}$	$0.19^{+0.22}_{-0.06}$
$Norm_{vapec1:superwind \text{ or } disk}^*$ ($\times 10^2$)	$7.9^{+9.3}_{-3.4}$	$1.7^{+4.8}_{-1.4}$
$kT_{vapec2:superwind \text{ or } disk}$ [keV]	0.62 ± 0.04	$0.57^{+0.08}_{-0.21}$
$Norm_{vapec2:superwind \text{ or } disk}^*$ ($\times 10^2$)	$6.6^{+3.8}_{-3.4}$	$0.5^{+0.8}_{-0.3}$
O/Fe †	24^{+9}_{-7}	27^{+9}_{-20}
Ne/Fe †	9.5 ± 2.4	$7.1^{+2.6}_{-6.1}$
Mg/Fe †	2.4 ± 0.7	$2.1^{+1.3}_{-0.9}$
Si/Fe †	$3.1^{+1.3}_{-1.2}$	$4.3^{+3.2}_{-2.0}$
$kT_{zbrems:superwind \text{ or } disk}^{\ddagger}$ [keV]	10 (fix)	10 (fix)
$Flux_{zbrems:superwind \text{ or } disk}^{\S}$ [$\times 10^{-14}$ erg s $^{-1}$ cm $^{-2}$]	8.4 ± 0.5	90^{+6}_{-4}
$\chi^2/d.o.f$	90/63	83/79

* Normalization of the *apec* model divided by a solid angle Ω , assumed in a uniform-sky ARF calculation (20' radius), i.e. $Norm = (1/\Omega) \int n_e n_H dV / (4\pi(1+z)^2 D_A^2)$ cm $^{-5}$ sr $^{-1}$ in unit of 10^{-14} , where D_A is the angular diameter distance.

† Number ratio relative to the Fe atom obtained from two-dimensional contour maps between Z and Fe.

‡ Temperature of the *zbrems* component.

§ Unabsorbed flux in the extracted region in 0.5–2 keV.

power law. The first two components represent emissions from the local area consisting of solar wind charge exchange (SWCX: e.g., Snowden et al. (2004)) and Local Hot Bubble (LHB) and Galactic halo (Milky Way Halo: MWH). On the other hand, the last component corresponds to the accumulation of unresolved extragalactic point sources (cosmic X-ray background: CXB) described by an absorbed power-law model with a photon index of 1.4 as shown in Kushino et al. (2002). Thus, we adopted the following models in the XSPEC software: $apec_{SWCX+LHB} + phabs_{Galactic} \times (apec_{MWH} + power-law_{CXB})$. We carried out a simultaneous fitting using the XIS0, 1 and 3 detectors at the energy range of 0.4–5.0 keV for the BI (XIS1) and 0.6–5.0 keV for the FIs (XIS0 and XIS3). For the XIS1 and XIS3 detectors, a constant factor denoted as f was multiplied to consider the systematic error in different sensors. Resulting spectra and parameters are shown in Figure 4 and Table 3. Resultant temperatures of the Galactic foreground and the surface brightness of the CXB component are consistent with typical values obtained in previous studies (e.g., Kushino et al. (2002); Yoshino et al. (2009)). The

data from the offset observations is also analyzed in Sato et al. (2010), which shows the best-fit parameters consistent with our results within the statistical errors.

3.2.2. Estimation of the stray light from the inner regions

Due to the poor *Suzaku* angular resolution (HPD \sim 1.8'), a stray light from the inner region has to be evaluated to derive physical properties of the hot ISM in the *halo* region properly. As the origin of the stray light, emissions from not only the *disk* region but also the nuclear region were taken into account because the nuclear region is extremely bright in hard X-ray due to the most intense starburst activity (Mitsuishi et al. 2011). As a stray light source, we firstly considered the emission from the nuclear region with a radius of 20'' based on Mitsuishi et al. (2011). The estimated count rate from the nuclear region is \sim 3% compared to NXB subtracted spectra in the *halo* region at the energy range between 0.5 and 5 keV. Therefore we concluded that the stray light from the nuclear region is negligible. Next, we extracted the whole disk region excluding the nuclear region by *XMM-Newton*. The spectrum was modeled well by two thin thermal plasmas and a bremsstrahlung with $\chi^2/d.o.f = 271/250$. The bremsstrahlung component from point sources dominates even in the soft band and metal abundances can not be constrained. Therefore, metal abundances of two thin thermal plasmas were set to be 1 solar. The estimated count rate from the stray light is \sim 20 % compared to NXB subtracted spectra in the *halo* region in 0.5–5 keV.

Thus, as the stray light source, these models were taken into account fixing all parameters to the best fit values in spectral analysis of the *halo* region.

3.2.3. Spectral fitting for the halo region

Spectra of the *halo* region were fitted with the X-ray background, hot interstellar gas (1 T or 2 T), a sum of point sources and the stray light from the disk modeled by $apec_{\text{SWCX+LHB}} + phabs_{\text{Galactic}} \times (apec_{\text{MWH}} + power-law_{\text{CXB}}) + phabs_{\text{Galactic}} \times phabs_{\text{halo}} \times (vapec_{1 T \text{ or } 2 T: \text{halo}} + zbrems_{\text{halo}}) + phabs_{\text{Galactic}} \times phabs_{\text{disk}} \times (apec_{2 T: \text{disk}} + zbrems_{\text{disk}})$. Parameters on the X-ray background were linked between NGC 253 and the offset region and consistent with those of the obtained only in the offset region within the statistical error. The fourth terms indicate the stray-light from the inner disk region.

Resultant spectra and the best fit parameters are shown in Figure 5 and Table 3. The goodness of the fit improved slightly by adding the second thermal component. The third thermal component was not required. The resultant temperature of the one-temperature model is almost consistent with that of the obtained by *XMM-Newton* (Bauer et al. 2008) while temperatures of the two-temperature model are about twice higher than those of Bauer et al. (2008). This discrepancy may be caused by the difference of the adopted energy band for spectral analysis. In Bauer et al. (2008), they adopted the energy band of 0.2–1.5 keV and no line feature of Mg and Si was observed owing to the lack of photons. As indicated in Figure 5, the higher temperature plasma with $kT \sim 0.6$ keV is responsible for emission lines such as Ne X, Mg XI and Si XIII. Abundance patterns for one- and two-temperature models were extracted as is the case of the *superwind* region and the *disk* region as shown in Table 3. Abundance patterns for both models are consistent with each other within the statistical error.

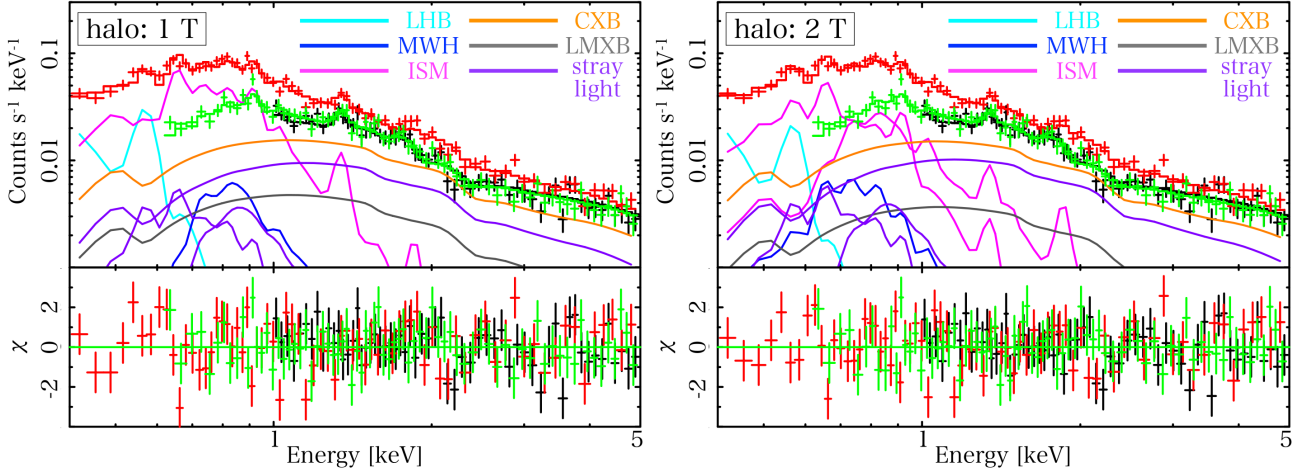


Fig. 5. NXB-subtracted XIS0 (black), XIS1 (red) and XIS3 (green) spectra observed by *Suzaku* at the energy range between 0.4 and 5.0 keV in the *halo* region. The lines show the best-fit model that consists of $apec_{\text{SWCX+LHB}}$ (cyan), $phabs_{\text{Galactic}} \times apec_{\text{MWH}}$ (blue), $phabs_{\text{Galactic}} \times power-law_{\text{CXB}}$ (orange), $phabs_{\text{Galactic}} \times phabs_{\text{halo}} \times (vapec_{1T \text{ or } 2T: \text{halo}} + zbremss_{\text{halo}})$ (magenta and gray) and $phabs_{\text{Galactic}} \times phabs_{\text{disk}} \times (apec_{2T: \text{disk}} + zbremss_{\text{disk}})$ (purple). The first three terms show the X-ray background which is composed of SWCX+LHB, MWH and CXB components and the forth and fifth terms indicate the ISM and the sum of point sources in the *halo* region. The last term corresponds to the stray light from the inner disk region. The X-ray background was linked between the offset region and the *halo* region. As the ISM component, one- (left) and two-temperature (right) models are adopted, respectively.

Resulting number ratios indicate that rich α elements exist even in the *halo* region, which suggests that metals in the *halo* region are provided by Type II supernovae associated with the inner starburst activity.

3.3. Surface brightness and hardness ratio

In this section, we investigated physical properties of the hot ISM such as density and temperature. To infer these physical parameters, we extracted surface brightness and hardness ratio. The soft band below 1 keV was used where the ISM component dominates as shown in Figure 5. We extracted the central bright rectangle region of $5.2' \times 13'$ (hereafter the *SB* region) along with the minor axis perpendicular to the disk (< 3 kpc from the center) toward the halo (3–10 kpc from the center) as shown in Figure 1 colored with cyan where higher S/N ratios were expected.

We extracted the surface brightness in two energy bands: 0.4–0.8 keV as the soft band and 0.8–1.0 keV as the hard band. The two energy bands are selected so that roughly the same number of photons are included. A contribution of the X-ray background, estimated from the simulation, was subtracted. To evaluate the contribution of the Galactic and CXB components, an observation of the background sky was simulated with the *xissim ftool*. We input the best fit parameters of spectral analysis obtained in the offset region (see second column of Table 3) into the simulation. The statistical error associated with the simulation is $< 3\%$ and hence negligible. For the estimation of the NXB component, we utilized the *xisnxbgen ftool*. These procedures allow us to extract information of

Table 3. Best fit parameters for the offset region and the *halo* region by *Suzaku*.

Region	Model	Halo	
		1T	2T
	f^* (XIS1)	$1.02^{+0.08}_{-0.07}$	$1.12^{+0.07}_{-0.06}$
	f^* (XIS3)	$0.95^{+0.08}_{-0.07}$	$0.93^{+0.06}_{-0.05}$
	$N_{\text{H } phabs:Galactic}$ ($\times 10^{21}$ [cm $^{-2}$])	0.15 (fix)	←
	$kT_{apec:SWCX+LHB}$ [keV]	$0.07^{+0.02}_{-0.01}$	$0.09^{+0.01}_{-0.02}$
	$Norm_{apec:SWCX+LHB}^{\dagger} / f$	227^{+996}_{-166}	84^{+169}_{-31}
	$kT_{apec:MWH}$ [keV]	$0.29^{+0.10}_{-0.06}$	$0.62^{+0.13}_{-0.41}$
	$Norm_{apec:MWH}^{\dagger} / f$	$1.7^{+1.1}_{-0.7}$	0.75 ± 0.26
	$\Gamma_{power-law:CXB}$ (fix)	1.4 (fix)	←
	$SB_{power-law:CXB}^{\ddagger}$	8.7 ± 0.5	8.6 ± 0.3
	$N_{\text{H } phabs:disk}$ ($\times 10^{21}$ [cm $^{-2}$])	0.5 (fix)	←
	$kT_{apec:disk1}$ [keV]	0.21 (fix)	←
	$Norm_{apec:disk1}^{\dagger} / f$	2.2 (fix)	←
	$kT_{apec:disk2}$ [keV]	0.73 (fix)	←
	$Norm_{apec:disk2}^{\dagger} / f$	0.53 (fix)	←
	$kT_{zbrems:disk}^{\S}$ [keV]	10 (fix)	←
	$Flux_{zbrems:disk}^{\#} / f [\times 10^{-13} \text{ erg s}^{-1} \text{ cm}^{-2}]$	1.3 (fix)	←
	$N_{\text{H } phabs:halo}$ ($\times 10^{21}$ [cm $^{-2}$])	<0.5	<0.7
	$kT_{vapec1:halo}$ [keV]	0.30 ± 0.02	0.22 ± 0.02
	O [Z $_{\odot}$]	$0.45^{+1.12}_{-0.21}$	$0.43^{+0.28}_{-0.14}$
	Ne [Z $_{\odot}$]	$0.60^{+1.43}_{-0.27}$	$0.84^{+0.74}_{-0.37}$
	Mg, Al [Z $_{\odot}$]	$1.1^{+0.94}_{-0.62}$	$1.2^{+1.2}_{-0.6}$
	Si, S, Ar, Ca [Z $_{\odot}$]	$1.2^{+5.4}_{-1.2}$	$1.3^{+1.8}_{-0.7}$
	Fe, Ni [Z $_{\odot}$]	$0.22^{+0.52}_{-0.13}$	$0.29^{+0.23}_{-0.11}$
	$Norm_{vapec1:halo}^{\dagger} / f$	43^{+38}_{-29}	36^{+46}_{-13}
	$kT_{vapec2:halo}$ [keV]		$0.59^{+0.19}_{-0.11}$
	$Norm_{vapec2:halo}^{\dagger} / f$		$11^{+9.1}_{-5.1}$
	O/Fe b	35^{+13}_{-9}	27^{+11}_{-9}
	Ne/Fe b	$6.8^{+1.8}_{-1.3}$	$7.1^{+2.4}_{-3.7}$
	Mg/Fe b	3.8 ± 1.2	$3.2^{+1.1}_{-1.0}$
	Si/Fe b	$3.5^{+3.4}_{-3.5}$	$3.2^{+1.9}_{-1.6}$
	$kT_{zbrems:halo}^{\S}$ [keV]	10 (fix)	←
	$Flux_{zbrems:halo}^{\#} / f [\times 10^{-14} \text{ erg s}^{-1} \text{ cm}^{-2}]$	$6.4^{+1.9}_{-1.8}$	$4.8^{+2.1}_{-2.0}$
	$\chi^2/d.o.f$	194/169	434/367

* Constant factor relative to the XIS0 detector.

\dagger Normalization of the *apec* model divided by a solid angle Ω , assumed in a uniform-sky ARF calculation (20' radius), i.e. $Norm = (1/\Omega) \int n_e n_H dV / (4\pi(1+z)^2 D_A^2) \text{ cm}^{-5} \text{ sr}^{-1}$ in unit of 10^{-14} , where D_A is the angular diameter distance.

\ddagger Surface brightness of the *power-law* model in the unit of photons $\text{s}^{-1} \text{ cm}^{-2} \text{ sr}^{-1} \text{ keV}^{-1}$ at 1 keV.

\S Temperature of the *zbrems* component.

$\#$ Unabsorbed flux in the extracted region in 0.5–2 keV.

b Number ratio relative to the Fe atom obtained from two-dimensional contour maps between Z and Fe.

the density and temperature of the ISM itself accurately. Then, for the Galactic and CXB components, a vignetting correction was carried out assuming a monochromatic energy in each energy band; 0.6 keV for the soft band and 0.9 keV for the hard band. We confirmed that this energy selection did not change our results significantly. Resultant surface brightness profiles after a background removal are shown in Figure 6 top. Its behavior seems to be different between the disk and the halo in the *SB* region. A slope in the disk is steeper than that of the halo in 0.4–0.8 keV while a bump-like structure is seen in the halo in 0.8–1.0 keV. To extract a hardness ratio profile, the surface brightness profile in 0.8–1 keV was divided by that in 0.4–0.8 keV. Resulting hardness ratio profile is shown in

Figure 6 bottom. A hardness ratio gradient is found in the disk while no hardness ratio gradient is observed in the halo. This suggests that a temperature gradient may exist only in the disk. To ensure this suggestion, an absorption effect that changes apparent hardness has to be taken into account. The neutral hydrogen gas is widely distributed from the central region to the halo (Koribalski et al. 1995). Its column density decreases gradually towards outside the disk from $\sim 5 \times 10^{21} \text{ cm}^{-2}$ around the central region to $\sim 5 \times 10^{20} \text{ cm}^{-2}$ around the border between the disk and the halo. Thus, the column density in the halo is estimated to be $< 5 \times 10^{20} \text{ cm}^{-2}$. Bauer et al. (2008) shows that significant extra absorption was not required in the SE disk and the halo of their paper, while additional absorption on the order of 10^{21} cm^{-2} was required in several regions of the NW disk. We also obtained using *XMM-Newton* that the 90 % upper limit of the absorption column density is $5 \times 10^{20} \text{ cm}^{-2}$ in the region corresponding to 2–5 bin in extracted profiles of the NW disk in the *SB* region. Variation on the hardness value due to extra absorption is within 5 % up to the column density of $1 \times 10^{21} \text{ cm}^{-2}$. Therefore, the gradient and the flatness on the hardness ratio profile is likely due to temperature difference. Only for the first bin of the NW disk in the *SB* region from the center may absorption affect the hardness ratio due to the densest molecular cloud on the order of $10^{23-24} \text{ cm}^{-2}$ (Sakamoto et al. 2011).

4. Discussion

4.1. Comparison with other starburst galaxies on abundance patterns

In §3.1 and §3.2, abundance patterns for three regions in NGC 253 are obtained. In this section, we compare abundance patterns of NGC 253 with those of other starburst galaxies, i.e., NGC 4631, M82 and NGC 3079, taken from the statistically best values of Yamasaki et al. (2009), Konami et al. (2011) and Konami et al. (2012). A comparison of abundance patterns is shown in Figure 7. Abundance patterns in the disk region of four starburst galaxies are consistent with one another and are heavily contaminated by SN II, probably associated with the starburst activity in the central region. Furthermore, abundance patterns of NGC 253 in the *halo* region are also SN II -like and consistent with those of NGC4631 and M82 in the halo, which suggests that the same chemical pollution mechanism works and that hot gas in the halo is provided by the central starburst region. In the case of NGC 3079, the abundance pattern in the halo is closer to that of solar. This result means that pollution may not be sufficient yet because NGC 3079 is considered to be in an early phase of the starburst (Konami et al. 2012).

4.2. Energetics of the halo region

We discuss the possibility that hot gas in the *halo* region may be energetically provided from the inner starburst region. In the *halo* region, observed unabsorbed luminosity and thermal energy ($3nkTV\eta/2$) of the hot gas in 0.5–10 keV are $(3.8_{-0.5}^{+2.4}$ and $2.3_{-0.7}^{+1.0}) \times 10^{38} \text{ erg s}^{-1}$ and $(2.2_{-0.6}^{+0.8}$ and $3.3_{-1.3}^{+2.5}) \times 10^{55} \eta^{1/2} \text{ erg}$ for low and high temperature plasmas in the best fit two-temperature model as shown in Table 3. We adopted a sum of the luminosity and the thermal energy of each plasma as the total observed luminosity and thermal energy. η (< 1) corresponds to the volume filling factor of

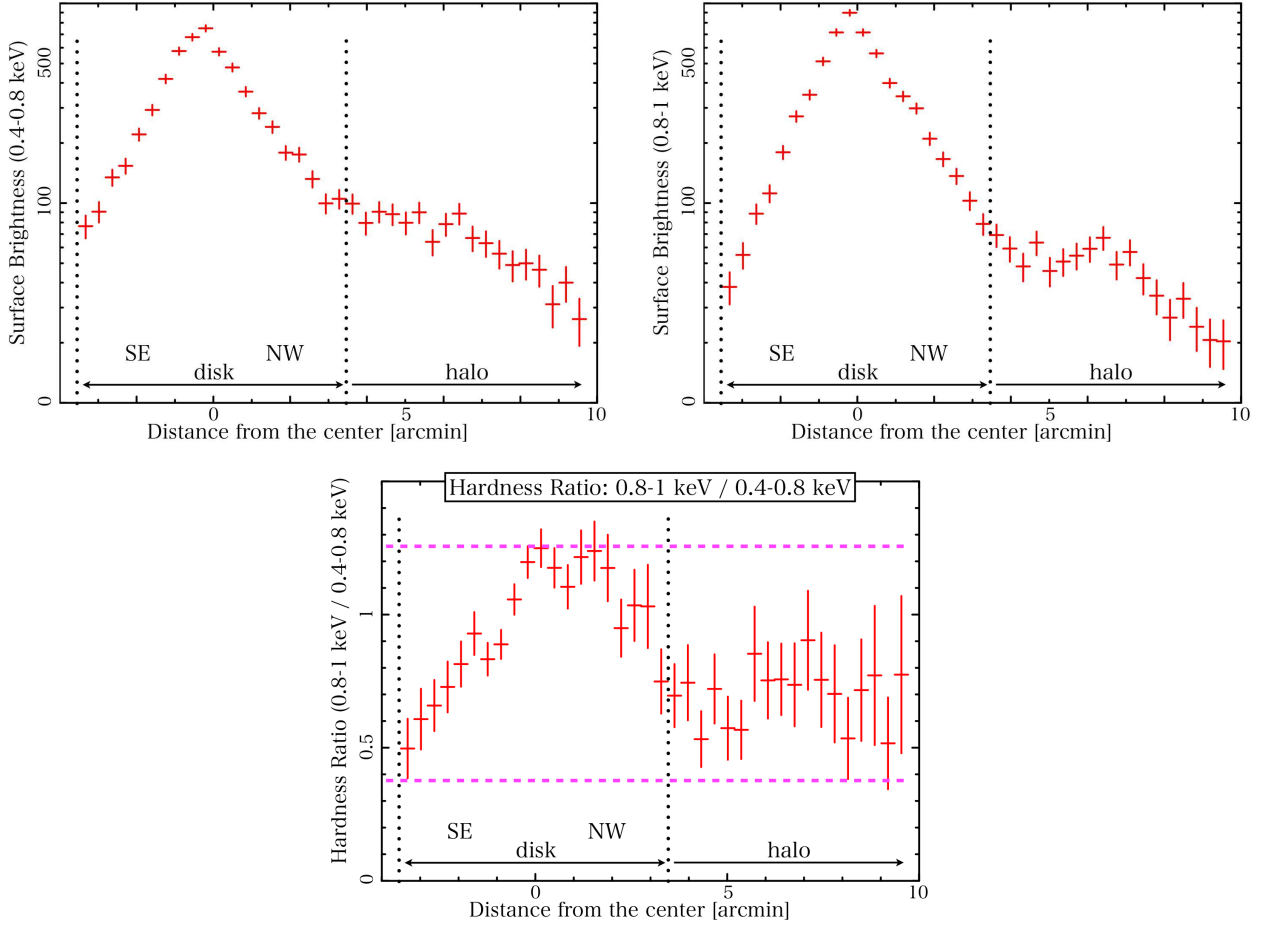


Fig. 6. Surface brightness after a background removal in the *SB* region at the energy range between 0.4 and 0.8 keV (top left) and 0.8 and 1.0 keV (top right) along with the minor axis perpendicular to the disk. Hardness ratio of 0.8–1.0 keV to 0.4–0.8 keV (bottom) was derived by dividing surface brightness profiles of each energy band. Dashed and dotted lines indicate corresponding temperatures of 0.2 and 0.6 keV assuming one-temperature thin thermal plasma with the absorption column density of $N_H = 5 \times 10^{20} \text{ cm}^{-2}$ and the border between the disk and the halo, respectively.

the X-ray emitting gas as shown in Cecil et al. (2002) and the same volume filling factor is assumed for both plasmas. The density is proportional to $\eta^{-1/2}$ and therefore the thermal energy is proportional to $\eta^{1/2}$. The lower limit of supernova rate around the nuclear region of NGC 253 are on the order of 0.1 yr^{-1} (Lenc & Tingay 2006). Assuming the typical starburst duration of 10^{6-7} yr , luminosity and thermal energy of a supernova of $10^{36-37} \text{ erg s}^{-1}$ and 10^{51-52} erg (Hughes et al. 1998), the expected total luminosity and thermal energy from supernovae during a starburst duration are calculated to be $10^{41-43} \text{ erg s}^{-1}$ and 10^{56-58} erg , respectively. Considering the total observed luminosity and thermal energy in the *halo* region, the energy of the observed thermal plasma may be supplied from the nuclear region if 0.01–50 $\eta^{1/2}$ % of the total emission in the nuclear region has flowed to the *halo* region. Note that from this discussion alone, we cannot constrain the contribution of other possible origins discussed in e.g., Heesen et al. (2009), Sharma et al. (2010) and Heesen et al. (2011).

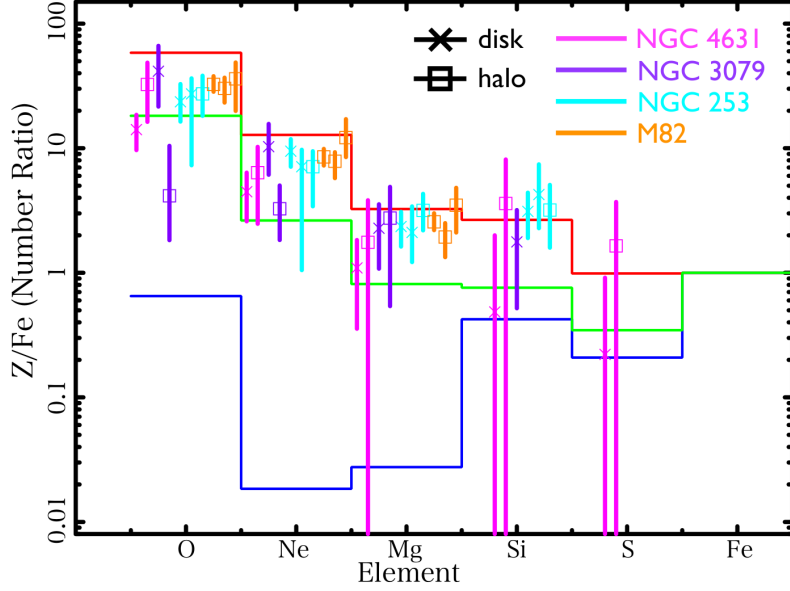


Fig. 7. Abundance patterns for starburst galaxies of NGC 4631 (magenta), NGC 3079 (purple), NGC253 (cyan) and M82 (orange), respectively. Cross and rectangle marks indicate the disk region and the halo region, respectively. For NGC 3079, we referred to abundance patterns of the central 0.5' circle and the 1'-2' ring region in Konami et al. (2012) as the disk and halo regions, respectively.

4.3. Dynamics of hot interstellar gas

In §3.3, surface brightness and hardness ratio profiles in the *SB* region were obtained. In order to examine dynamics of hot interstellar gas, we extracted information on the density and temperature in the disk and the halo of NGC 253 from the profiles. Firstly, we derived the temperature profile from the hardness ratio profile as shown in Figure 8 top. The hardness ratio is converted to the temperature assuming a thin thermal plasma model (*vapex* in the XSPEC software) multiplied by the absorption column density of $5 \times 10^{20} \text{ cm}^{-2}$ convolved with the *Suzaku* response matrix. Metal abundances are fixed to the best fit values in the best fit model as shown in Table 3. The temperature in the halo of the *SB* region is about 0.3 keV which is consistent with the obtained by the one-temperature model of spectral analysis in the *halo* region as indicated in Table 3. The temperature ranges from 0.2 keV to 0.6 keV. These temperatures are also consistent with the obtained by the two-temperature model in spectral analysis which reflect typical temperatures with differential emission measure in the *disk* region and the *halo* region. Thus, it is indicated that the resultant temperature profile traces the typical temperature of the ISM under the assumption of the one-temperature model.

Next, information on the density was extracted. The surface brightness can be expressed by $\Lambda(T) n_e n_H V \sim \Lambda(T) n_H^2 V$, where $\Lambda(T)$, n_e , n_H and V indicate emissivity, electron and hydrogen densities and volume, respectively. To calculate the volume we need the length of the hot gas in line-of-sight direction. Since we do not know the actual size, here we simply assume that the line-of-sight length is the same in the extracted *SB* region. In this case, the surface brightness of each projected

region is proportional to the density squared and the emissivity (dependent on temperature). Here we assume that the volume filling factor is unity. We extracted the emissivity in 0.4–0.8 keV as is the case with Gastaldello et al. (2007) using XSPEC assuming the temperature and abundances obtained from the hardness ratio and spectral fitting as shown in Table 2 and 3, respectively.

Finally, we plotted the hardness ratio and the surface brightness as shown in Figure 8 bottom. As reference values, polytropic indices ($T\rho^{1-\gamma} = \text{const}$) of 6/3, 5/3 and 4/3 between the density and temperature are plotted together. The observed gradient between the hardness ratio and the surface brightness can be expressed by the curve with the polytropic index of 5/3 for both the NW disk and the SE disk. We confirmed that the best-fit polytropic indices are $1.5^{+0.1}_{-0.4}$ and $1.6^{+0.2}_{-0.3}$ for the NW disk region and the SE disk region, respectively. Equation of state of hot gas with polytropic index of 5/3 corresponds to be adiabatic. In contrast, the surface brightness declines gradually in the halo of the SB region with a shallower slope compared to that of the disk keeping hardness ratios constant. This suggests that the hot interstellar gas expands from the inner disk adiabatically towards the halo and then expands freely from the inner part of the halo towards the outer part of the halo as the outflow.

4.4. Constraint on the velocity of the outflow in the halo

In §4.3, it is suggested that the hot gas expands freely from the inner part of the halo towards the outer part of the halo as the outflow and no temperature gradient is detected in the halo of the SB region, which indicates that any effective cooling processes does not work significantly. Even through the density in the halo is small, the X-ray emitting gas cools throughout the radiative cooling, which requires that the hot gas has to proceed at a certain level of the velocity towards the outer part of the halo to reproduce the observed flat temperature profile. The temperature gradient in the halo of the SB region was calculated to be $(0.3 \pm 1.6) \times 10^{-2}$ [keV / kpc] + 0.32 ± 0.09 [keV]. To extract the lower limit of the velocity of hot interstellar gas, we adopted the slope of -1.3×10^{-2} [keV / kpc] as a 90 % lower limit and 0.40 keV as a starting point. Assuming the following three conditions, we constrained the velocity of the hot interstellar gas in this section: (1) the ISM gas moves with a constant velocity in the halo, (2) the ISM gas cools through the radiative cooling process and (3) the density profile was estimated from the observed surface brightness profile in 0.4–0.8 keV. In this model, during a specific time period Δt [s], hot gas loses an energy of $\sim \Delta t \times n(R)\Lambda(T)$ leading to a temperature decrease satisfying the following relation:

$$T(t + \Delta t) = T - \Delta t \frac{n(R)\Lambda(T)}{k}, \quad (1)$$

where k , $n(R)$ and $\Lambda(T)$ are Boltzmann constant, the density of hot gas and cooling rate in units of erg K^{-1} , cm^{-3} and $\text{erg cm}^{-3} \text{ s}^{-1}$, respectively. A density profile is obtained from the surface brightness profile in 0.4–0.8 keV assuming a diameter of 5.2'; and a height of 21'' for a bin. We adopt a cylindrical emitting region for a steady state outflow. The density profile is exhibited in Figure 9. Resulting density in both the central region and the halo are consistent with previous works within a factor of 2 (Pietsch et al. 2001; Bauer et al. 2007; Bauer et al. 2008). We confirmed that systematic errors of the density due to the assumption of spectral parameters are less than 10 %. The density profile was

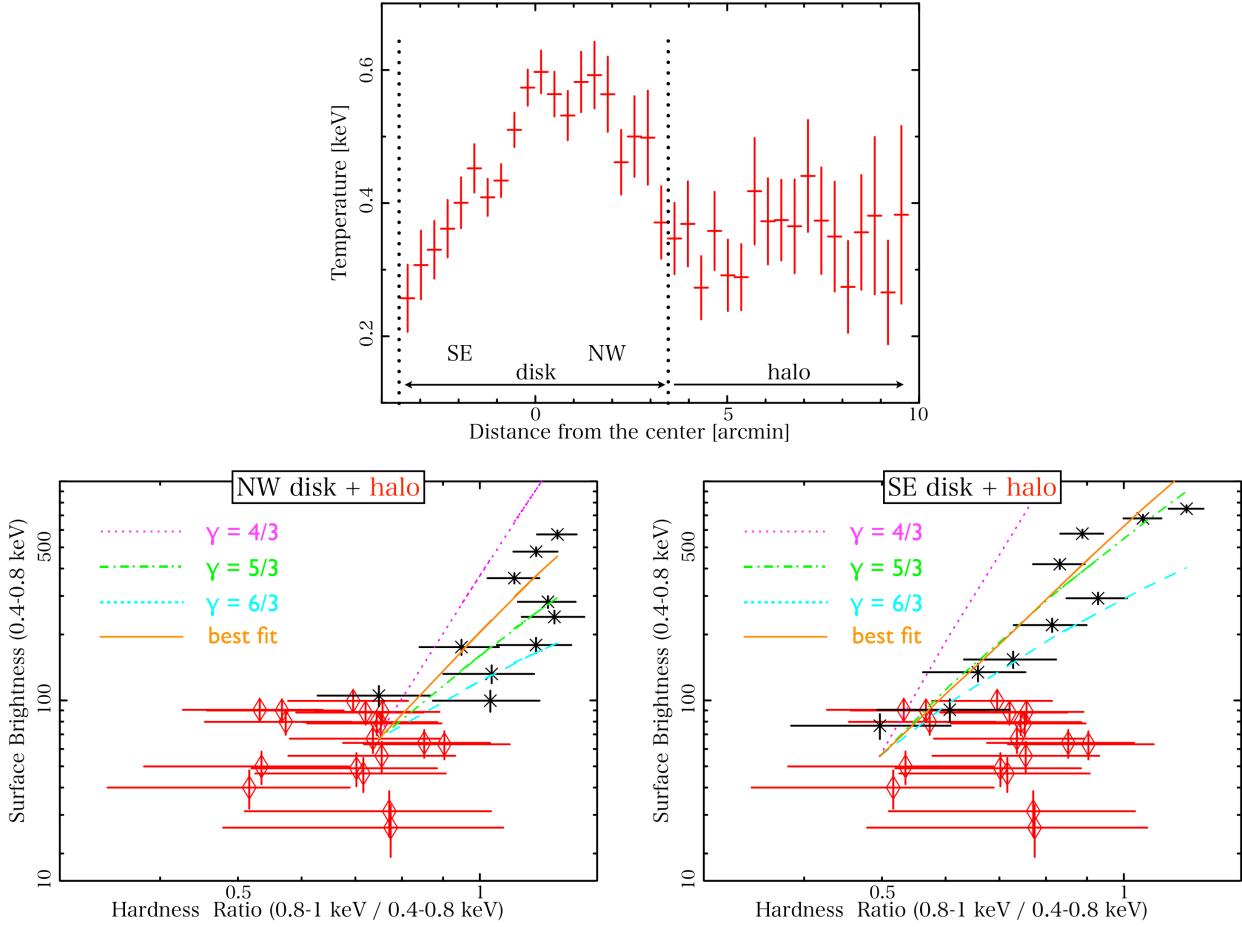


Fig. 8. Top: temperature profile obtained from the hardness ratio profile in the *SB* region assuming the simplest model of the absorbed thin thermal plasma with the column density of $5 \times 10^{20} \text{ cm}^{-2}$. Hardness ratio vs the surface brightness at the energy range between 0.4 and 0.8 keV in the NW disk (bottom left) and the SE disk (bottom right). Cross and diamond marks show results in the disk and the halo, respectively. As reference values, polytropic indices of 6/3 (dash), 5/3 (dot-dash) and 4/3 (dot) and the best fit curves (solid) between density and temperature are also plotted together. The normalization of each curve is arbitrarily determined.

represented empirically with the double exponential model as shown in Figure 9 upper right. This smoothed empirical density function and radiative cooling rate by Sutherland & Dopita (1993) are used for the calculation of temperature decrease as show in equation (1). We utilized cooling rate assuming CIE with the abundance ratio of $[\text{Fe}/\text{H}] = -0.5$ considering our spectral analysis (see Table 3). We interpolated emissivity between discrete values assuming linearity. A comparison between the observed and the expected temperature profiles is shown in Figure 10. We also plotted the observed lowest temperature gradient within 90 % confidence level. Thus, it is suggested that the velocity of 100 km s^{-1} is required as the lower limit to reproduce the observed temperature profile. Considering the escape velocity of NGC 253, $\sim 220 \text{ km s}^{-1}$ (Puche et al. 1991; Hlavacek-Larrondo et al. 2011), it is suggested that once the ISM gas reaches the edge of the halo it can escape from the host galaxy breaking out its gravitational potential by adding the thermal velocity to the outflow velocity. It should

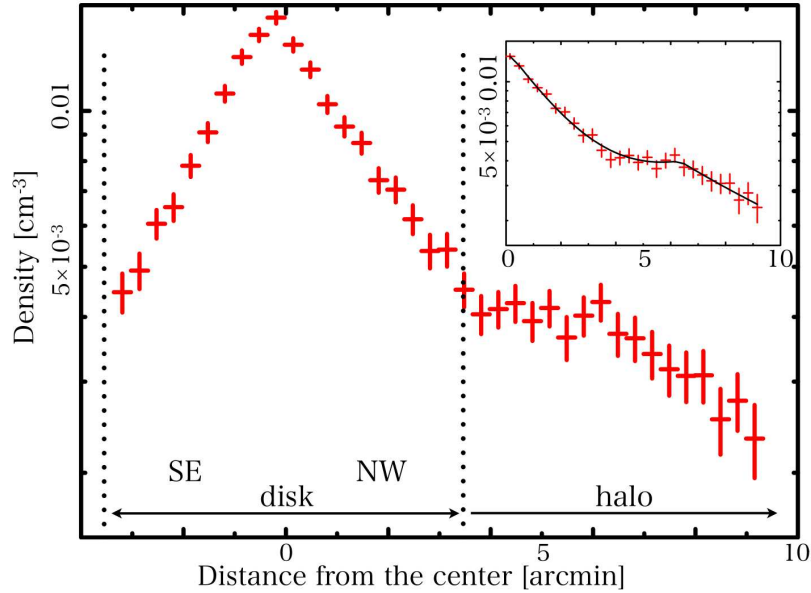


Fig. 9. Density profile estimated by the surface brightness profile in the *SB* region at the energy range between 0.4 and 0.8 keV as shown in Figure 6 top left. Upper right in this figure shows the density profile in the NW disk and the halo fitted with the double exponential function.

be noted that $\eta < 1$ is naturally expected, although the exact value is hard to know in particular in the halo region. Actually, the optical image of NGC 253 (Strickland & Stevens 2000; Matsubayashi et al. 2009; Westmoquette et al. 2011) suggests that the gas is clumpy at least in the disk region. Recent numerical simulations (e.g., Strickland & Stevens (2000); Cooper et al. (2009)) also indicates clumpy structure. In the case of $\eta < 1$, the required velocity is even larger because the density and hence the cooling rate increases with $\eta < 1$.

5. Conclusions

X-ray properties of the hot interstellar gas in starburst galaxy NGC 253 was investigated through abundance patterns, the surface brightness and the hardness ratio. We conducted spectral analysis for three regions in NGC 253, i.e., the *superwind* region, the *disk* region and the *halo* region, characterized by multiwavelength observations. Various emission lines such as O, Ne, Mg, Si and Fe were observed in all three regions. We extracted abundance patterns of O/Fe, Ne/Fe, Mg/Fe and Si/Fe. Resulting abundance patterns of all four elements are consistent in the three regions within the statistical error, which suggests that the origin of the hot interstellar gas in three regions is identical. Abundance patterns in the *halo* region are heavily contaminated by type II supernovae and therefore it is indicated that the hot interstellar gas in the *halo* region is provided by the central starburst activity. The energetics considering the observed luminosity and thermal energy in the *halo* region also can support this indication on condition that 0.01–50 $\eta^{1/2}$ % of the total emission in the nuclear region has flowed to the *halo* region.

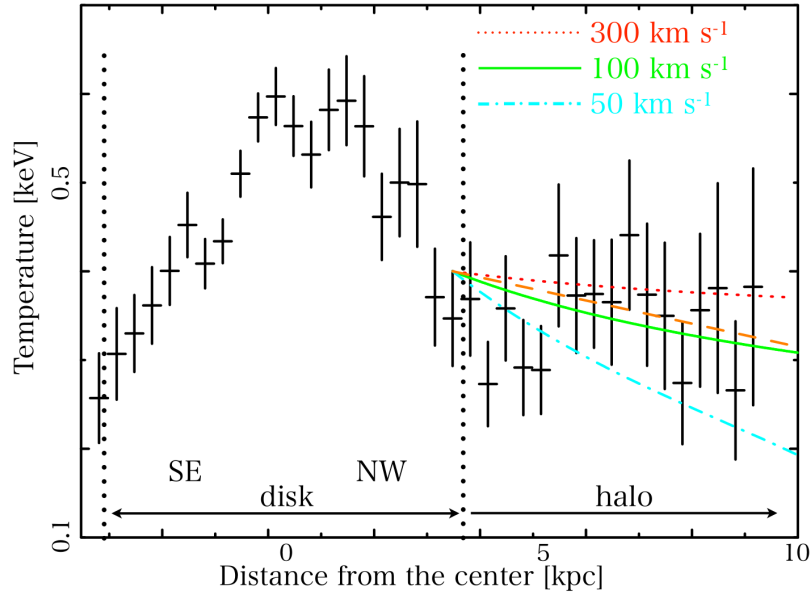


Fig. 10. Comparison between the observed temperature profile and the expected temperature profile in the halo of the *SB* region through the radiative cooling process with constant velocities of 300 km s^{-1} (dot), 100 km s^{-1} (solid) and 50 km s^{-1} (dot-dash), respectively. Dashed line indicates the observed lowest temperature gradient within the 90 % confidence level.

The hardness ratio and the surface brightness in the *SB* region show a different behavior between the disk and the halo. The polytropic index (γ) of $5/3$ in $T\rho^{1-\gamma} = \text{const}$ relation seems to be preferable at the hot disk of $<3 \text{ kpc}$ from the center along with the minor axis while no gradient was seen in the halo whose distance is between 3 and 10 kpc from the center but the surface brightness decreased gradually towards the outside. These results indicate the following physical picture that the hot interstellar gas expands adiabatically in the disk and then moves as free expansion from the inner part of the halo towards the outer part of the halo as the outflow. Finally, we constrained the velocity of this outflow in the halo. Assuming that the hot gas cools through radiative cooling and moves with the constant velocity in the halo, the velocity of $>100 \text{ km s}^{-1}$ is required to reproduce the observed temperature profile. Considering the escape velocity $\sim 220 \text{ km s}^{-1}$ of NGC 253, it is suggested that if the hot interstellar gas reaches the edge of the halo region hot interstellar gas can escape from the gravitational potential of NGC 253 as the outflow by combining the outflow velocity and the thermal velocity.

Acknowledgement

I. M. is grateful to Kentaro Someya and Prof. Kazuhisa Mitsuda for useful advice of spectral analysis to extract abundance patterns and discussion to constrain the outflow velocity. Part of this work was financially supported by the Ministry of Education, Culture, Sports, Science and Technology, Grant-in Aid for Scientific Research 10J07487, 15340088 and 22111513.

References

- Aguirre, A. and Hernquist, L. and Schaye, J. and Weinberg, D. H. and Katz, N. and Gardner, J. 2001, *ApJ*, 560, 599
- Anders, E., & Grevesse, N. 1989, *gca*, 53, 197
- Bauer, M., Pietsch, W., Trinchieri, G., Breitschwerdt, D., Ehle, M., Freyberg, M. J., & Read, A. M. 2008, *AAP*, 489, 1029
- Bauer, M., Pietsch, W., Trinchieri, G., Breitschwerdt, D., Ehle, M., & Read, A. 2007, *A&A*, 467, 979
- Cecil, G., Bland-Hawthorn, J., & Veilleux, S. 2002, *ApJ*, 576, 745
- Cooper, J. L., Bicknell, G. V., Sutherland, R. S., & Bland-Hawthorn, J. 2009, *ApJ*, 703, 330
- Dalcanton, J. J., et al. 2009, *ApJS*, 183, 67
- Gastaldello, F., Buote, D. A., Humphrey, P. J., Zappacosta, L., Bullock, J. S., Brighenti, F., & Mathews, W. G. 2007, *ApJ*, 669, 158
- Heckman, T. M., 2003, *Revista Mexicana de Astronomia y Astrofisica Conference Series*, 17, 47
- Heesen, V., Beck, R., Krause, M., & Dettmar, R.-J. 2009, *Astronomische Nachrichten*, 330, 1028
- . 2011, *A&A*, 535, A79
- Hlavacek-Larrondo, J., Carignan, C., Daigle, O., de Denus-Baillargeon, M.-M., Marcelin, M., Epinat, B., & Hernandez, O. 2011, *MNRAS*, 411, 71
- Hughes, J. P., Hayashi, I., & Koyama, K. 1998, *ApJ*, 505, 732
- Ishisaki, Y., et al. 2007, *PASJ*, 59, 113
- Iwamoto, K., Brachwitz, F., Nomoto, K., Kishimoto, N., Umeda, H., Hix, W. R., & Thielemann, F.-K. 1999, *ApJS*, 125, 439
- Kalberla, P. M. W., Burton, W. B., Hartmann, D., Arnal, E. M., Bajaja, E., Morras, R., & Pöppel, W. G. L. 2005, *A&A*, 440, 775
- Kaneda, H., Yamagishi, M., Suzuki, T., & Onaka, T. 2009, *ApJL*, 698, L125
- Kennicutt, Jr., R. C. 1998, *ApJ*, 498, 541
- Konami, S., Matsushita, K., Gandhi, P., & Tamagawa, T. 2012, *ArXiv e-prints*
- Konami, S., Matsushita, K., Tsuru, T. G., Gandhi, P., & Tamagawa, T. 2011, *PASJ*, 63, 913
- Koribalski, B., Whiteoak, J. B., & Houghton, S. 1995, *PASA*, 12, 20
- Kushino, A., Ishisaki, Y., Morita, U., Yamasaki, N. Y., Ishida, M., Ohashi, T., & Ueda, Y. 2002, *PASJ*, 54, 327
- Lenc, E. and Tingay, S. J. 2006, *AJ*, 132, 1333
- Lumb, D. H., Warwick, R. S., Page, M., & De Luca, A. 2002, *A&A*, 389, 93
- Matsubayashi, K., Sugai, H., Hattori, T., Kawai, A., Ozaki, S., Kosugi, G., Ishigaki, T., & Shimono, A. 2009, *ApJ*, 701, 1636
- Mitsuishi, I., Yamasaki, N. Y., & Takei, Y. 2011, *ApJL*, 742, L31
- McQuinn, K. B. W., Skillman, E. D., Cannon, J. M., Dalcanton, J., Dolphin, A., Hidalgo-Rodríguez, S., Holtzman, J., Stark, D., Weisz, D. & Williams, B. 2010, *ApJ*, 724, 49
- Nomoto, K., Tominaga, N., Umeda, H., Kobayashi, C., & Maeda, K. 2006, *Nuclear Physics A*, 777, 424
- Origlia, L., Ranalli, P., Maiolino, R., & Comastri, A. 2005, in *Astrophysics and Space Science Library*, Vol. 329, *Starbursts: From 30 Doradus to Lyman Break Galaxies*, ed. R. de Grijs & R. M. González Delgado, 56P
- Pence, W. D. 1980, *ApJ*, 239, 54

Pettini, M., Shapley, A. E., Steidel, C. C., Cuby, J.-G., Dickinson, M., Moorwood, A. F. M., Adelberger, K. L., & Giavalisco, M. 2001, *ApJ*, 554, 981

Pietsch, W., Vogler, A., Klein, U., & Zinnecker, H. 2000, *A&A*, 360, 24

Pietsch, W., et al. 2001, *A&A*, 365, L174

Puche, D., Carignan, C., & van Gorkom, J. H. 1991, *AJ*, 101, 456

Sakamoto, K., Mao, R.-Q., Matsushita, S., Peck, A. B., Sawada, T., & Wiedner, M. C. 2011, *ApJ*, 735, 19

Sato, K., Kelley, R. L., Takei, Y., Tamura, T., Yamasaki, N. Y., Ohashi, T., Gupta, A., & Galeazzi, M. 2010, *PASJ*, 62, 1423

Sharma, M., Nath, B. B., & Shchekinov, Y. 2011, *ApJL*, 736, L27

Shapley, A. E., Steidel, C. C., Pettini, M., & Adelberger, K. L. 2003, *ApJ*, 588, 65

Snowden, S. L., Collier, M. R., & Kuntz, K. D. 2004, *ApJ*, 610, 1182

Songaila, A., & Cowie, L. L. 1996, *AJ*, 112, 335

Strickland, D. K., Heckman, T. M., Weaver, K. A., & Dahlem, M. 2000, *AJ*, 120, 2965

Strickland, D. K., & Stevens, I. R. 2000, *MNRAS*, 314, 511

Strickland, D. 2002, *Astronomical Society of the Pacific Conference Series*, 253, 387

Strickland, D. K., Heckman, T. M., Colbert, E. J. M., Hoopes, C. G., & Weaver, K. A. 2004, *ApJS*, 151, 193

Sutherland, R. S., & Dopita, M. A. 1993, *ApJS*, 88, 253

Tawa, N., et al. 2008, *PASJ*, 60, 11

Ulvestad, J. S., & Antonucci, R. R. J. 1997, *ApJ*, 488, 621

Veilleux, S., Cecil, G., & Bland-Hawthorn, J. 2005, *ARA&A*, 43, 769

Westmoquette, M. S., Smith, L. J., & Gallagher, III, J. S. 2011, *MNRAS*, 414, 3719

Yamasaki, N. Y., Sato, K., Mitsuishi, I., & Ohashi, T. 2009, *PASJ*, 61, 291

Yoshino, T., et al. 2009, *PASJ*, 61, 805